Ultrahigh Energy-Storage in Dual-Phase Relaxor Ferroelectric Ceramics

Xin Xiong, Hui Liu, Ji Zhang, Lucas Lemos da Silva, Zhonghui Sheng, Yonghao Yao, Ge Wang, Manuel Hinterstein, Shujun Zhang, and Jun Chen**

Hui Liu, Xin Xiong, Yonghao Yao, Jun Chen
Department of Physical Chemistry, Beijing Advanced Innovation Center for Materials Genome Engineering, University of Science and Technology Beijing, Beijing 100083, China
E-mail: huiliu@ustb.edu.cn; junchen@ustb.edu.cn

Ji Zhang
Nanjing University of Science and Technology, Nanjing 210094, China

Lucas Lemos da Silva, Manuel Hinterstein
Fraunhofer Institute for Mechanics of Materials IWM, 79108 Freiburg, Germany

Zhonghui Sheng
Wuhan University of Technology, Wuhan, 430070, China

Ge Wang
University of Manchester, Manchester S13 9PL, United Kingdom

Shujun Zhang
University of Wollongong, Wollongong, NSW 2500, Australia

Jun Chen
Hainan University, Haikou 570228, China

Keywords: dielectric energy-storage ceramics, dual-phase structure, relaxor ferroelectrics, perovskite

Abstract

High-performance dielectric energy-storage ceramics are beneficial for electrostatic capacitors used in various electronic systems. However, the trade-off between reversible polarizability and breakdown strength poses a significant challenge in simultaneously achieving high energy density and efficiency. Here we present a strategy to address this issue by constructing a dual-phase structure through in-situ phase separation. We develop $(Bi_{0.5}Na_{0.5})TiO_3$-$BaTiO_3$-based relaxor ferroelectric ceramics, creating a grain-separated dual perovskite phase structure using

a facile solid-state reaction method. These ceramics feature two interactive relaxor phases with diversified nanoscale polar structures and heterogeneous grain boundaries, synergistically contributing to high polarization with low hysteresis, substantially increased resistivity, and suppressed electrostrain. Remarkably, we achieve a record-high energy density of 23.6 J cm^{-3} with a high efficiency of 92% under 99 kV mm^{-1} in the bulk ceramic capacitor. This strategy holds promise for enhancing overall energy-storage performance and related functionalities in ferroelectrics.

1. Introduction

Dielectric energy-storage ceramic capacitors can store electrical energy through electrostatic field, enabling ultrafast charge-discharge rates. [1-4] They serve as essential components in advanced high-power systems, finding application in various fields, such as electric vehicles, electronic gadgets, and smart power grids. [5-7] As technological advancements forge ahead, there is an increasing need to develop the next generation of dielectric ceramic capacitors with high energy density (W_{rec}) to facilitate device miniaturization and integration in cutting-edge applications. [8, 9] Simultaneously, these capacitors must maintain high efficiency (η) to minimize energy dissipation and ensure operational reliability. [10-13]

The energy-storage performance of a dielectric is determined by the electric-field induced polarization behavior and breakdown strength (E_B). To achieve high energy density and efficiency, a dielectric material should ideally exhibit a combination of high maximum polarization (P_m), minimal hysteresis (H), and high E_B. Perovskite-structured relaxor ferroelectric (RFE) ceramics, renowned for their high reversible polarizability due to nanoscale domain structures, have been extensively studied for energy-storage applications. [5] Chemical compositional design to regulate the heterogeneous polar structure is the most prevalent strategy for developing RFE solid solution ceramics with improved energy-storage performance. [14-16] Additionally, various strategies based on electrical characteristics and preparation technologies have been employed to enhance E_B. [17-19] Consequently, numerous RFE ceramics have been explored, leading to significant energy density advancements in recent years. However, owing to the inherent trade-off between critical parameters, such as P_m *vs.* E_B, and P_m *vs.* H, the energy density of conventional dielectric bulk ceramic capacitors is limited (< 15 J cm^{-3}) if a high efficiency (> 90%) is pursued. Currently, the highest W_{rec} value of 18.5 J cm^{-3} has been achieved in $NaNbO_3$ (NN)-based bulk ceramic, while its η is below 80% at maximum electric

field of 99.5 kV mm^{-1}. [20] Simultaneously achieving high energy density and efficiency remains a significant challenge in bulk ceramic capacitors.

Composite structures that leverage the unique properties of different constituents to address the inverse correlation between properties and enhance overall performance have been widely utilized in polymers, metals, and other materials. [21] For example, dielectric polymer composites can effectively balance the trade-off between P_m and E_B, leading to improved energy-storage performance. [22] However, designing perovskite ceramic composites presents challenges. Traditional methods of introducing foreign substances can result in intercalation into the lattice matrix due to the high chemical flexibility of the perovskite structure. This often results in a degradation of the electric properties, causing a reduction in overall polarization and increased loss. Unexpected composition segregation has been observed in some compositionally complex solid-solution perovskite ceramics due to the considerable difference in ion characteristics. [23, 24] We refer to this process as in-situ phase separation, which involves the simultaneously reaction and separation of different components. For instance, core-shell structures and precipitate phases have been reported in some $BiFeO_3$-$BaTiO_3$ (BF-BT)-based, $(Bi_{0.5}Na_{0.5})TiO_3$ (BNT)-based, and $BaTiO_3$ (BT)-based ceramics prepared through traditional solid sintering method. [17, 25-27] Interestingly, these composite structures formed naturally via in-situ phase separation often exhibit enhanced macroscopic electrical properties. Therefore, in-situ phase separation would be a feasible method for constructing perovskite ceramic composites to enhance the overall energy-storage performance.

Herein we employ the in-situ phase separation strategy to generate dual perovskite phase RFE ceramics, thereby mitigating the inverse correlation between reversible polarizability and breakdown strength. We demonstrate that an ultrahigh W_{rec} of 23.6 J cm^{-3} accompanied with high η of 92% under electric field of 99 kV mm^{-1}, can be obtained in BNT-BT-based dual perovskite phase relaxor ferroelectric ceramics, surpassing the state-of-the-art bulk dielectric ceramics. This work provides a new strategy, beyond the prevalent chemical composition design approach, for designing perovskite-type RFE ceramics for advanced energy-storage applications.

2. Results and Discussion

2.1 Microstructure of dual perovskite phase relaxor ferroelectric ceramics

To experimentally realize a dual-phase structure, we selected the $(Bi_{0.5}Na_{0.5})TiO_3$-$BaTiO_3$ (BNT-BT)-based system as a model due to its relatively high polarization and complicated *A*-site chemical disorder. Initial nominal compositions of (0.6-*x*)BNT-0.4BT-*x*$CdZrO_3$ (BNT-BT-*x*CZ) were designed. The incorporation of CZ was motivated by two factors: the small ionic radii of Cd^{2+} (1.31 Å) compared to that of Ba^{2+} (1.61 Å) and Na^{+} (1.39 Å), potentially resulting in a large lattice mismatch and phase separation, and the use of *B*-site Zr^{4+} ions to induce relaxor characteristics. We fabricated the ceramics by using a conventional solid-state reaction method according to the stoichiometric ratio and employed the synchrotron X-ray diffraction (SXRD) to identify the composition-dependent structure. Incorporating CZ into BNT-40BT leads to the evolution from a single tetragonal phase to two sets of perovskite phase diffraction patterns, each displaying symmetrical single peaks (**Figure 1**a and Figure S1). This indicates phase separation and the formation of a dual pseudocubic perovskite phase structure. Significantly, this composite structure differs from the commonly reported combination of a perovskite phase and a non-perovskite phase. [18, 28] The pseudocubic phase with a larger lattice parameter was labeled as C1, while the phase with a smaller lattice parameter was designated as C2. As the CZ content increases, there is a corresponding increase in the relative fraction of the C2 phase.

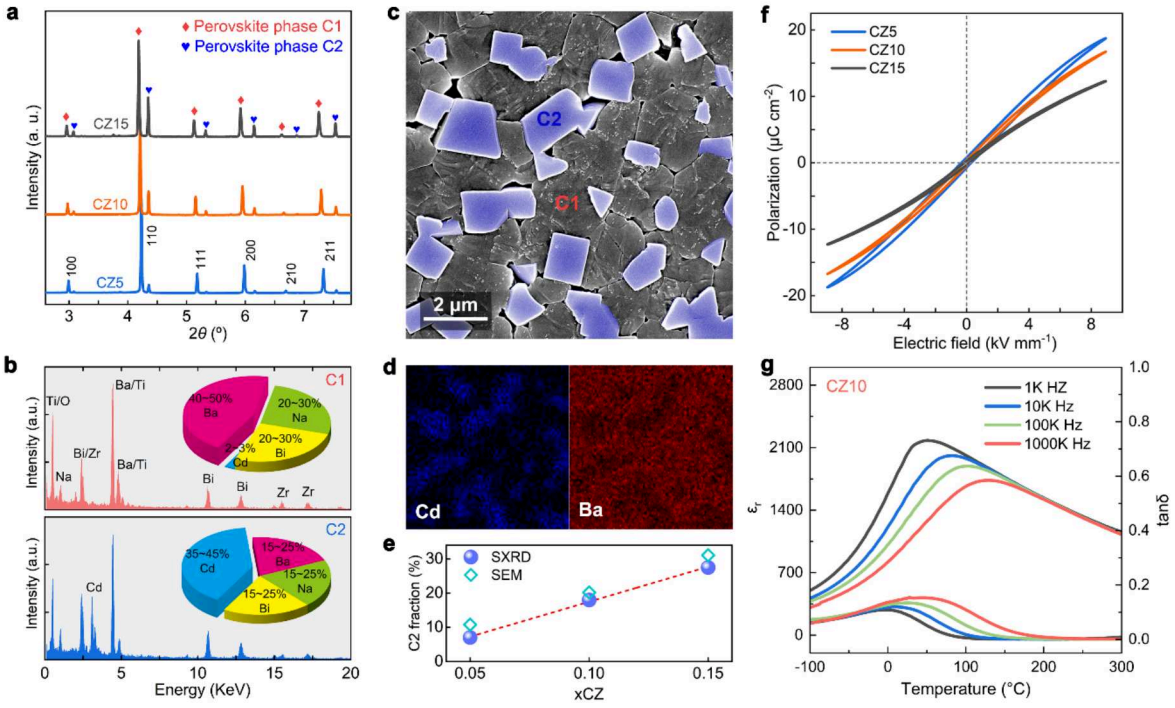

Figure 1. (a) Synchrotron X-ray diffraction patterns. (b) EDS patterns recorded from each phase along with chemical composition analysis. (c) SEM micrograph from the polished and acid etched surface and (d) the corresponding element distribution of CZ10 ceramic. (e)

Calculated volume fraction of C2 phase. (f) Polarization–electric field (*P*-*E*) hysteresis loops. (g) Dielectric spectrum of CZ10 ceramic.

To investigate the microstructure and chemical composition of dual-phase ceramics, we utilized electron microscope equipped with element analysis (Figure 1b-d, Figure S2-S3). Two types of grains were identified - the larger polyhedral grains corresponding to the C1 phase, and the smaller square-shaped grains belonging to the C2 phase. The C1 and C2 phase grains exhibit a random distribution, with isolated C2 grains initially embedded in the C1 matrix, forming 0-3-type composites at low CZ content. As the C2 phase fraction increases, the isolated C2 grains are gradually connected with each other, forming 3-3-type composite. These two types of assemblies exhibit distinct grain boundaries, which will influence their electrical breakdown characteristics. Based on the recorded element distribution and energy dispersive spectrum (EDS) (Figure 1b and Figure S3), the main element separation is observed for the Cd and Ba. The C1 phase contains a higher concentration of Ba, while C2 phase contains a higher concentration of Cd. The rough chemical compositions of the C1 and C2 phases in dual-phase ceramics with varying CZ content, determined through EDS and SXRD profile fitting, are presented in Table S1. The occurrence of the chemically complex composition of the C2 phase would be due to the entropy stabilization effect. Notably, the *A*-site configurational entropy of C2 phase is as high as 1.3*R*, much higher than the 1.0*R* that in the C1 phase. This increased entropy serves to decrease the free energy, thereby rendering the phase insoluble in the mixture and leading to the macroscopic phase separation. The perovskite structure of both phases was also confirmed by electron diffraction patterns (Figure S4). Notably, ½(*ooe*) superstructure spots were detected in C2 phase while not in the C1 phase. This could be attributed to the long-range oxygen octahedral tilting or the *A*-site chemical ordering, caused by the large size differences between Ba, Bi, Cd, and Na ions in the C2 phase. We used the $Pm\bar{3}m$ and $Im\bar{3}$ cubic model respectively for the C1 and C2 phase to fit the SXRD patterns (Figure S5), and yielded a good fit (Figure S6). The volume fractions of the C2 phase were calculated to be 7%, 18%, and 27% for CZ5, CZ10, and CZ15, respectively (Figure 1e). These values align with the results quantified by the area ratio of different phases in the SEM images (Figure S3). Thus, grain-separated dual-phase ceramics featuring two pseudocubic perovskite phases can be obtained through a conventional solid-state reaction method without any specialized treatments, owing to in-situ phase separation. We measured the ferroelectric and dielectric properties of the dual-phase ceramics (Figure 1f-g, and Figure S7-S8). The BNT-40BT exhibits ferroelectric behavior with relaxor features due to its highly disordered *A*-site cations. The incorporation of

CZ leads to a transition from FE state to RFE state with narrow *P-E* loops. The dual-phase ceramics exhibit a maximum polarization (P_m) in the range of 12 to 20 μC cm^{-2} with hysteresis below 10% at 9 kV mm^{-1}. In contrast to the typical phenomenon where the presence of secondary phases in perovskite ferroelectrics leads to an increased hysteresis, the grain-scaled mixture dual-phase structure in these ceramics actually reduces hysteresis. Despite a notable decrease in P_m compared to BNT-40BT, the dual-phase ceramics still demonstrate higher polarization values compared to other nearly hysteresis-free RFEs. [1, 10] The RFE characteristics in these dual-phase ceramics can be additionally validated by the broad diffuseness and frequency-dependent dielectric maxima (Figure S8). It is worth noting that unlike sandwich-type composites where the dielectric spectrum shows a combination of distinct components, [29, 30] there is no such behavior observed in these dual-phase ceramics. This suggests a strong coupling between the two perovskite phases. Higher CZ content leads to a slight reduction in hysteresis and polarization. Among the compositions studied, CZ10 exhibits a relatively large polarization of 16.8 μC cm^{-2} and minimized hysteresis of 6.5% at 9 kV mm^{-1}, therefore detailed structure analysis were conducted for this critical composition.

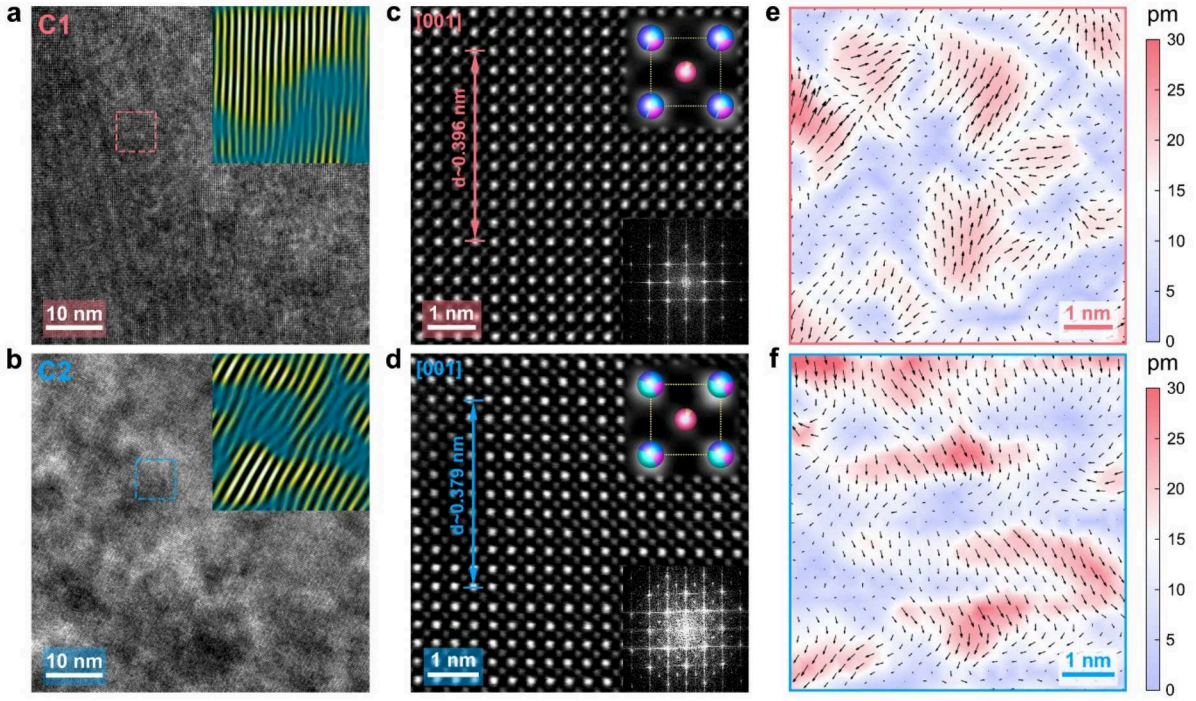

Figure 2. Nanoscale structures of dual-phase CZ10 ferroelectric ceramic. (a) and (b) HR-TEM images recorded along $[110]_c$ direction. The insets indicate the IFFT patterns from the selected areas. (c) and (d) HAADF images recorded along $[001]_c$, along with (e) and (f) the atomic displacement vector mapping. The insets in c and d indicate the *A*-site and *B*-site in the unit cell and the FFT diffraction patterns.

The domain structures of the dual-phase ferroelectric ceramic of CZ10 were probed using high-resolution transmission electron microscopy (**Figure 2**). Despite the absence of long-range ferroelectric domains structure, a light and shade contrast indicative of a nanoscale domain structure was observed in both types of grains (Figure 2a-b). Ordered lattices were observed in both phases, with the C2 exhibiting significantly stronger lattice distortions than the C1 phase which is due to its stronger size mismatch. We performed high-angle annular dark-field scanning transmission electron microscopy (HAADF-STEM) to examine the polar structures of both phases along the $[001]_c$ zone (Figure 2c-d). The C1 and C2 grains can be clearly distinguished by the lattice spacing directly measured from the HADDF images and the corresponding FFT patterns. The C2 phase is characterized by a smaller lattice parameter of 3.79 Å in comparison to the 3.96 Å observed in the C1 phase, and it displays ½(*ooe*) superstructure spots. The polar displacement vector is considered by the deviation of the *B/A*-site atoms with reference to the nearest four *A*/*B*-site atoms in the HADDF images (Figure S9). Island-like coherent regions, approximately 1-2 nm in size and exhibiting diverse symmetries occur in the C1 phase (Figure 2e). In contrast, the C2 phase contains relatively larger and elongated island-type clusters, around 3-5 nm in size, with *R* symmetry (Figure 2f). Therefore, both perovskite phases exhibit a nanoscale heterogeneous polar structure, a prominent characteristic of RFEs. It is recognized that small-sized polar clusters typically reduce polarization anisotropy, resulting in a more flattened domain-reorientation pathway that effectively minimizes hysteresis loss. [1, 13, 14] The grain-separated dual-phase structure provides additional polarization diversity compared with that in single phase, further lowering the domain switching barrier.

2.2. Energy-storage properties in bulk ceramic capacitors

We evaluated the energy-storage performance of CZ10 bulk ceramic by conducting unipolar *P*-*E* loops measurements. Slim *P*-*E* loops were observed under various electric field amplitudes (Figure S10). Specifically, a large P_m of 75 μC cm^{-2} along with small P_r of 8 μC cm^{-2} were obtained at an ultrahigh electric field of 99 kV mm^{-1} (**Figure 3**a-b). The obtained E_B was much higher compared to other bulk ceramics (Figure 3d). It is generally believed that E_B is inversely related to the thickness of the dielectric materials, [31] with higher values observed in thinner sample, our current measurements are performed on samples with 54 μm in thickness and electrodes of 1 mm in diameter. Remarkably, the E_B in CZ10 is comparable to that of MLCCs with much thinner single ceramic layers (~5–20 μm). This resulted in an ultrahigh W_{rec} of 23.6 J cm^{-3} with an excellent efficiency of 92% (Figure 3b), outperforming the recently extensively

studied dielectric ceramics, including bulk ceramics and MLCCs (Figure 3c-e). For example, it surpasses the previously reported record W_{rec} value of 18.5 J cm^{-3} and η of 78.5% in NN-based relaxor bulk ceramics, [20] as well as the MLCCs based on textured BNT-SBT (21.5 J cm^{-3}, 80%), [3] high-entropy BT (20.8 J cm^{-3}, 97.5%), [1] $AgNbO_3$ (AN) (14 J cm^{-3}, 85%), [32] and NN (12.6 J cm^{-3}, 88%). [33] It is worth noting that even at a high electric field of 99 kV mm^{-1}, there is no sign of polarization saturation observed, suggesting that higher energy-storage could be achieved in MLCCs due to their thinner single ceramic layers that allow them to withstand even higher electric fields.

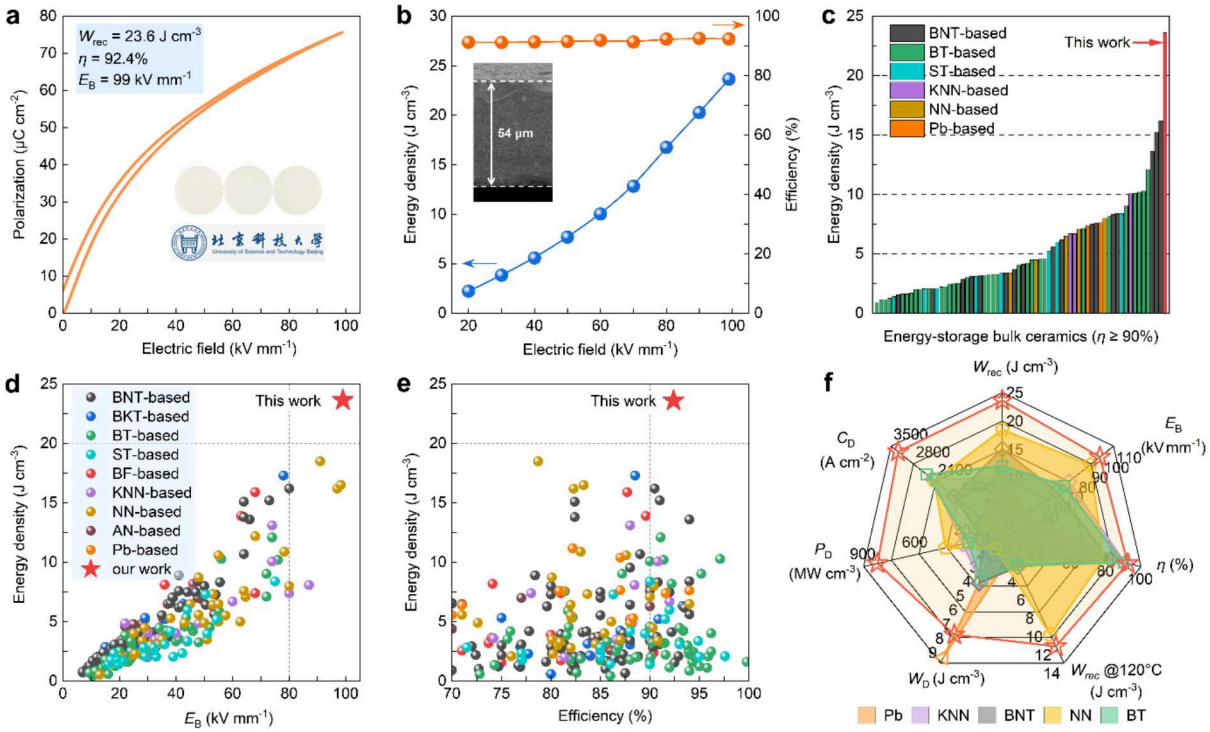

Figure 3. Energy-storage capabilities of dual-phase CZ10 ferroelectric ceramic. (a) Unipolar *P-E* loop under breakdown field. (b) W_{rec} and η with respect to applied electric fields. The inset shows the cross-section SEM image of ceramic sample showing the thickness of the bulk ceramic capacitor. Comparison of (c) W_{rec} with $\eta \geq 90\%$, (d) E_B versus W_{rec}, (e) W_{rec} versus η, and (f) comprehensive performance with representative bulk ceramic capacitors.

The temperature stability and cycling reliability are crucible for practical energy storage applications, which were also assessed under electric field of 60 kV mm^{-1} (Figure S11). An excellent temperature stability was observed with less than 10% variation in W_{rec} up to 180 °C. However, as the temperature increases, the hysteresis also increases, resulting in a decrease in efficiency, being on the order of 80% at 180 °C. Additionally, the CZ10 bulk ceramic demonstrates excellent cycling reliability, with a minimal degradation (below 3% variations) in

energy density and efficiency after up to 10^6 cycles. Additionally, the CZ10 bulk ceramic exhibits a high discharge energy density (W_D) of 7.0 J cm^{-3}, a fast discharge rate ($t_{0.9} \approx 25$ ns), a high current density (C_D) of 3280 A cm^{-2}, and an ultrahigh power density (P_D) of 820 MW cm^{-3} at 50 kV mm^{-1} (Figure S12). Besides, it exhibits excellent mechanical property with a high Vickers hardness of 11 GPa (Figure S13). Overall, the CZ10 dual-phase ceramic surpasses currently reported bulk ceramics in terms of comprehensive energy-storage properties (Figure 3f), and shows high potential for use in the dielectric capacitors.

2.3. Origins of dual-phase structure to overcome polarizability and breakdown strength trade-off

To understand the role of the dual-phase structure in generating reversible high polarizability, and thus contributing to the high energy-storage performance, we utilized *in-situ* electrical biasing high-energy synchrotron X-ray diffraction (SXRD) to investigate the structural changes in the CZ10 dual-phase ceramic (**Figure 4**a-d). Facilitated by the high-energy X-rays, the transmission mode in this technique can provide the intrinsic information in bulk ceramics while minimizing surface effects. A dual-phase structure can be obviously detected from the bulk ceramic. Under a bipolar cyclic electric field, the peak positions and intensities of both phases undergo fully reversible changes (Figure 4a-c). As the electric field increases, the positions of the (200) and (210) reflections shift to lower angles, indicating electric field-induced lattice strain. Interestingly, a broadening of the (200) reflection occurs under high electric fields (Figure S14), suggesting a transformation from pseudocubic symmetry with highly dynamic PNRs to long-range FE ordering featuring with lattice distortion. Additionally, the peak intensity of the (210) reflection increases, akin to the phenomenon observed in BNT-based materials during electric-field induced RFE-to-FE transformation. [34] This suggests that both phases actively respond to the electric-field and contribute to macroscopic polarization. Notably, dual perovskite structures are preferable to conventional composite structures that incorporate non-perovskite phases such as simple oxides, nitrides, or Aurivillius phases with low susceptibility. [35, 36] The latter often reduces the macroscopic polarization and increased loss.

To distinguish the different behavior in C1 and C2 phases under external electric field, the lattice strains (ε) were calculated, where the ε in C2 phase is slightly higher compared to C1 phase, leading to a matched interface at the grain boundary (Figure S15). Negligible hysteresis is observed in the calculated lattice strain curves, indicating the structural evolution is reversible.

The calculated total lattice strain is as low as 0.065% and 0.07% respectively for C1 and C2 phases under 8 kV mm^{-1} (Figure 4d). Additionally, the electrostrictive coefficient Q_{33} is 0.028 m^{4}C^{-2} (Figure S16), which is a relatively low among relaxor ferroelectric ceramics. [37] These features are beneficial for achieving a high E_B. [3] We also examined the temperature-dependent structure evolution of the dual-phase ceramic using high-resolution SXRD. No significant changes in symmetry or onset of symmetrical single peak were observed across the temperature range from 160 K to 500 K (Figure 4e), confirming the pseudocubic phase characteristic for RFEs. Importantly, both phases exhibited similar lattice variations (Figure 4f), contributing to the good temperature stability in this dual-phase ferroelectric ceramic. The synergistic structural changes between these two phases result in high polarization with minimal hysteresis and excellent temperature stability.

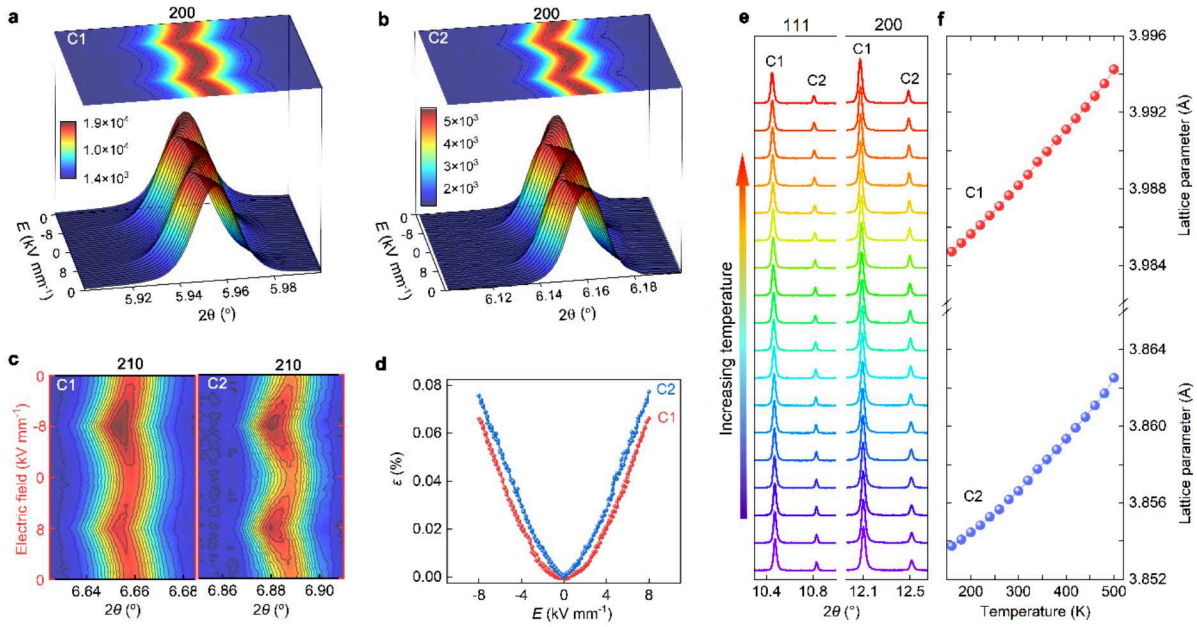

Figure 4. In-situ synchrotron X-ray diffraction analysis under electric field and temperature of dual-phase CZ10 ceramic. In-situ contour plots of (a,b) (200) peak and (c) (210) peak with the electric field. (d) Calculated electric field-induced lattice strain. (e) Temperature-dependent SXRD patterns from 160-500 K, and (f) calculated lattice parameter of each phase.

The electrical microstructures were explored to reveal the role of the dual-phase structure in achieving ultrahigh E_B in bulk ceramics. The Weibull distribution of E_B were plotted with varying CZ content (**Figure 5**a). The calculated E_B initially increased and then decreased, with a maximum value of 99 kV mm^{-1} observed in CZ10. Despite the relatively lower E_B values of 47 kV mm^{-1} and 72 kV mm^{-1} were observed for CZ5 and CZ15, respectively, these values are still at a relatively high level compared to other bulk ceramics. Notably, the C2 phase exhibits

a smaller grain size of about 1.5 μm compared to the 2.5 μm grain size of the C1 phase (Figure S2). By introducing the C2 phase that refines the average grain size, the proportion of grain boundary can be increased, thereby enhancing the overall breakdown strength. However, there is no significant difference in the overall grain size among these three dual-phase ceramics, indicating that the E_B could also be related to the phase ratio of the two phases.

We used impedance spectroscopy to probe the electrical characteristics of the ceramics (Figure S17). Impedance complex plane plots at 510 °C fitted with resistor–capacitor element are shown in Figure 5b. The total resistivity of the ceramics can be obtained from the low frequency intercept of the arc on the Z' axis. The dual-phase ceramics exhibit high total resistivity, especially for CZ10, reaching 7.8 $M\Omega \cdot cm^{-1}$, much higher than other bulk ceramics (Figure 5c), being conducive to a higher intrinsic breakdown strength. We further analyzed the impedance and modulus spectroscopy (Figure 5d and Figure S18) to evaluate the electrical homogeneity of dual-phase ceramics. For CZ10, the Z'' and M'' peaks appear at almost the same frequency, indicating an almost ideal Debye response, suggesting good electrical homogeneity. [17] In contrast, CZ15 shows a large gap in the spectrum, indicating a considerable electrical non-uniformity within the ceramic. On the other hand, the M'' peaks of CZ0 and CZ5 exhibit varying degrees of non-ideal high-frequency tails, indicating the presence of larger volume fractions of C1 grains that act as more conductive pathways—an undesirable characteristic. This scenario is also supported by the electric tree simulated using phase-field simulation (Figure 5e). Compared with CZ10, CZ5 shows a higher likelihood of conducting within C1 grains, and CZ15 within C2 grains, leading to material breakdown. Essentially, the C1-C2 grain boundaries exhibit a superior intrinsic breakdown strength compared to the C1-C1 or C2-C2 grain boundaries. This indicates that constructing a dual-phase system with an appropriate phase ratio can effectively reduce the volume fraction of conductive pathways, thereby boosting the material's resistance to breakdown. Such enhanced breakdown resistance can be highly beneficial for high-voltage capacitors. Additionally, the dual-phase structure suppresses lattice strain, and reduces the probabilities of the crack-driven dielectric breakdown. The synergistic effect of the dual-phases produces a “1+1>2” effect for realizing high E_B.

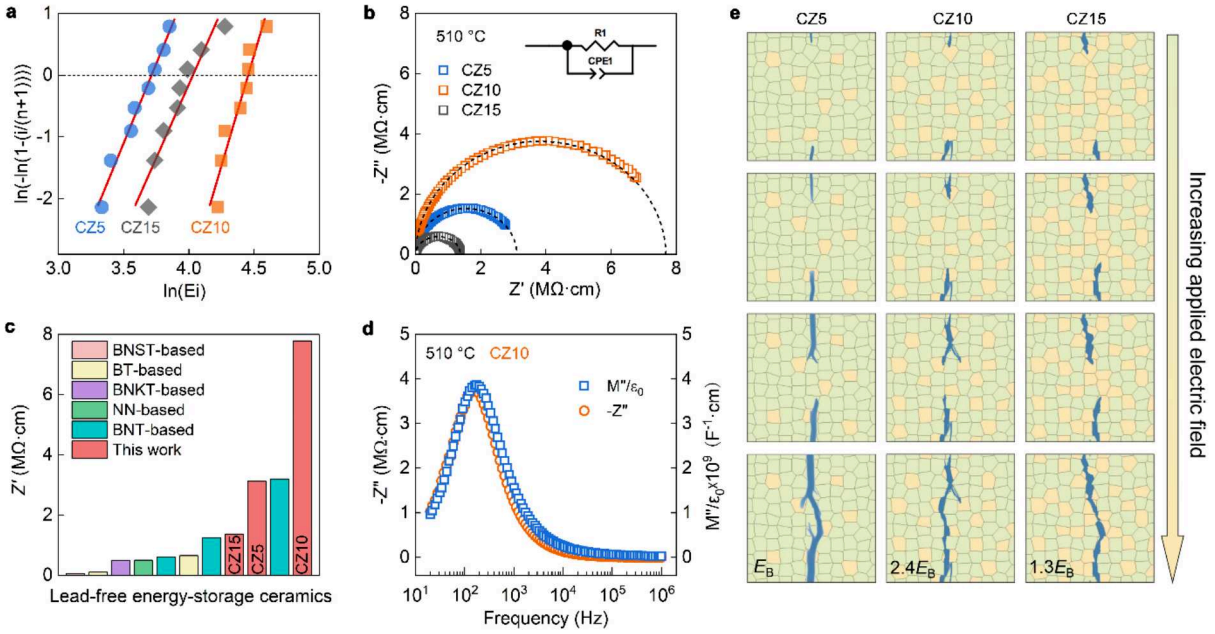

Figure 5. Electrical microstructures of dual-phase ferroelectric ceramics. (a) Weibull distribution of the breakdown electric field. (b) Z^* plots at 510 °C. (c) Comparison of total electrical resistivity at around 510 °C. (d) Spectroscopic plots of Z'' and M'' spectra at 510 °C of the CZ10 ceramic. (e) Breakdown path images based on phase-field simulations.

3. Conclusion

Our strategy of constructing dual perovskite phase RFE ceramics through *in-situ* phase separation has been demonstrated to enable the attainment of high reversible polarizability and a substantial enhancement of the breakdown strength simultaneously. Benefiting from the synergistic effects of gain- separated two RFE phases, an ultrahigh W_{rec} of 23.6 J cm^{-3} with an excellent η of 92% under electric field of 99 kV mm^{-1} has been realized in bulk ceramic capacitors. Employing the mismatch of ions with different ionic radii, valence states and ferroelectric activity to generate in-situ phase separation and construct dual-perovskite phase microstructure is expected to be applicable to other type dielectric energy-storage capacitors and could be universal to related functionalities.

4. Experimental Section

Sample preparation: BNT-BT-based dual-phase ferroelectric ceramics were prepared by conventional solid-state reaction method. For details of the synthesis procedure can be referred to the Supporting Information.

Characterization: The energy storage properties were measured on bulk ceramic samples with thickness in 50-60 μm, and gold electrodes with an area of approximately 0.8 mm^2. The discharge characteristics, with an overdamped value of 51 Ω, were measured using Tongguo (TG) technology (CFD-003, China). The dielectric temperature spectrum were measured by a dielectric spectrum measurement system (LDM-500, BALAB, China). The electrochemical impedance were tested by a precision impedance analyzer (4294A, Agilent, USA).

In-situ high-energy SXRD measurements were performed at the P02.1 beamline of the PETRA III facility by using an X-ray wavelength of 0.2074 Å with a Varex XRD 4343CT 2D detector at a distance from the sample of 2200 mm. High-resolution SXRD of CZ10 ceramic were measured at BL02B2 beamline of SPring-8 with Debye-Scherrer camera (λ = 0.42 Å) from 160 K – 500 K.

Surface topography images of acid etched ceramic sample were captured by a field-emission scanning electron microscope (LEO1530, ZEISS SUPRA 55, Germany). Atomic-scale high-angle annular dark-field (HAADF) phase images were acquired by a STEM (JEM-F200, JEOL, Japan) equipped with probe and image aberration-correction operated at 200 kV.

An electrostatic breakdown model was employed to dynamically simulate the breakdown process based on phase field theory. The details can be seen in the the Supporting Information.

Supporting Information

Supporting Information is available from the Wiley Online Library or from the author.

Acknowledgements

This work was financially supported by Key research and development Program of Ministry of Science and Technology of China (No. 2022YFB3204000), the Outstanding Young Scientists Program of Beijing Higher Education Institutions (JWZQ20240101015), the National Natural Science Foundation of China (Grant Nos. 22235002, 22075014 and 52372121), and and the Fraunhofer Internal Program (Attract 40-04857). We acknowledge DESY (Hamburg, Germany), a member of the Helmholtz Association HGF, for the provision of experimental facilities. Parts of this research were carried out at PETRA III and we would like to thank Martin Etter and Alexander Schoekel for assistance in using beamline P02.1. Beamtime was allocated for proposal I-20230129. The HR-SXRD experiments were performed at the BL02B2 beamline of SPring-8 with the approval of the Japan Synchrotron Radiation Research Institute.

Competing interests

Authors declare that they have no competing interests.

Data availability

The data that support the findings of this study are available from the corresponding author upon reasonable request.

Received: ((will be filled in by the editorial staff))
Revised: ((will be filled in by the editorial staff))
Published online: ((will be filled in by the editorial staff))

References

[1] M. Zhang, S. Lan, B. B. Yang, H. Pan, Y. Q. Liu, Q. H. Zhang, J. L. Qi, D. Chen, H. Su, D. Yi, Y. Y. Yang, R. Wei, H. D. Cai, H. J. Han, L. Gu, C.-W. Nan, Y.-H. Lin, *Science* **2024**, 384, 185.

[2] Z. Sun, H. Liu, J. Zhang, H. Luo, Y. Yao, Y. Zhang, L. Liu, J. C. Neuefeind, J. Chen, *J. Am. Chem. Soc.* **2024**, 146, 13467.

[3] J. L. Li, Z. H. Shen, X. H. Chen, S. Yang, W. L. Zhou, M. W. Wang, L. H. Wang, Q. W. Kou, Y. C. Liu, Q. Li, Z. Xu, Y. F. Chang, S. J. Zhang, F. Li, *Nat. Mater.* **2020**, 19, 999.

[4] J. Kim, S. Saremi, M. Acharya, G. Velarde, E. Parsonnet, P. Donahue, A. Qualls, D. Garcia, L. W. Martin, *Science* **2020**, 369, 81.

[5] A. R. Jayakrishnan, J. P. B. Silva, K. Kamakshi, D. Dastan, V. Annapureddy, M. Pereira, K. C. Sekhar, *Prog. Mater. Sci.* **2023**, 132, 101046.

[6] G. Wang, Z. L. Lu, Y. Li, L. H. Li, H. F. Ji, A. Feteira, D. Zhou, D. W. Wang, S. J. Zhang, I. M. Reaney, *Chem. Rev.* **2021**, 121, 6124.

[7] L. T. Yang, X. Kong, F. Li, H. Hao, Z. X. Cheng, H. X. Liu, J. F. Li, S. J. Zhang, *Prog. Mater. Sci.* **2019**, 102, 72.

[8] Z. Sun, J. Zhang, H. Luo, Y. Yao, N. Wang, L. Chen, T. Li, C. Hu, H. Qi, S. Deng, L. C. Gallington, Y. Zhang, J. C. Neuefeind, H. Liu, J. Chen, *J. Am. Chem. Soc.* **2023**, 145, 6194.

[9] Z. H. Yao, Z. Song, H. Hao, Z. Y. Yu, M. H. Cao, S. J. Zhang, M. T. Lanagan, H. X. Liu, *Adv. Mater.* **2017**, 1601727.

[10] P. Y. Zhao, Z. M. Cai, L. L. Chen, L. W. Wu, Y. Huan, L. M. Guo, L. T. Li, H. Wang, X. H. Wang, *Energy Environ. Sci.* **2020**, 13, 4882.

[11] H. F. Ji, D. W. Wang, W. C. Bao, Z. L. Lu, G. Wang, H. J. Yang, A. Mostaed, L. H. Li, A.

Feteira, S. K. Sun, F. F. Xu, D. J. Li, C. J. Ma, S. Y. Liu, I. M. Reaney, *Energy Storage Mater.* **2021**, 38, 113.

[12] H. Liu, Z. Sun, J. Zhang, H. J. Luo, Q. H. Zhang, Y. H. Yao, S. Q. Deng, H. Qi, J. Liu, L. C. Gallington, J. C. Neuefeind, J. Chen, *J. Am. Chem. Soc.* **2023**, 145, 11764.

[13] H. Pan, S. Lan, S. Q. Xu, Q. H. Zhang, H. B. Yao, Y. Q. Liu, F. Q. Meng, E. J. Guo, L. Gu, D. Yi, X. R. S. Wang, H. B. Huang, J. L. MacManus-Driscoll, L. Q. Chen, K. J. Jin, C. W. Nan, Y. H. Lin, *Science* **2021**, 374, 100.

[14] B. B. Yang, Q. H. Zhang, H. B. Huang, H. Pan, W. X. Zhu, F. Q. Meng, S. Lan, Y. Q. Liu, B. Wei, Y. Q. Liu, L. T. Yang, L. Gu, L. Q. Chen, C. W. Nan, Y. H. Lin, *Nat. Energy* **2023**, 8, 956.

[15] H. Liu, Z. Sun, J. Zhang, H. J. Luo, Y. P. Zhang, A. Sanson, M. Hinterstein, L. J. Liu, J. C. Neuefeind, J. Chen, *J. Am. Chem. Soc.* **2024**, 146, 3498.

[16] N. N. Luo, K. Han, M. J. Cabral, X. Z. Liao, S. J. Zhang, C. Z. Liao, G. Z. Zhang, X. Y. Chen, Q. Feng, J. F. Li, Y. Z. Wei, *Nat. Commun.* **2020**, 11, 4824.

[17] G. Wang, J. L. Li, X. Zhang, Z. M. Fan, F. Yang, A. Feteira, D. Zhou, D. C. Sinclair, T. Ma, X. L. Tan, D. W. Wang, I. M. Reaney, *Energy Environ. Sci.* **2019**, 12, 582.

[18] F. Yan, J. Qian, J. F. Lin, G. L. Ge, C. Shi, J. W. Zhai, *Small* **2024**, 20, 2306803.

[19] A. W. Xie, J. Fu, R. Z. Zuo, X. W. Jiang, T. Y. Li, Z. Q. Fu, Y. W. Yin, X. G. Li, S. J. Zhang, *Adv. Mater.* **2022**, 34, 2204356.

[20] J. Jiang, X. J. Meng, L. Li, S. Guo, M. Huang, J. Zhang, J. Wang, X. H. Hao, H. G. Zhu, S. T. Zhang, *Energy Storage Mater.* **2021**, 43, 383.

[21] H. H. Wu, F. P. Zhuo, H. M. Qiao, L. K. Venkataraman, M. P. Zheng, S. Z. Wang, H. Huang, B. Li, X. P. Mao, Q. B. Zhang, *Energy Environ. Mater.* **2022**, 5, 486.

[22] M. Z. Yang, M. F. Guo, E. R. Xu, W. B. Ren, D. Y. Wang, S. Li, S. J. Zhang, C. W. Nan, Y. Shen, *Nat. Nanotechnol.* **2024**, 19, 588.

[23] D. Y. Suárez-Sandoval, P. K. Davies, *Appl. Phys. Lett.* **2003**, 82, 3215.

[24] K. B. Xi, J. C. Liu, B. B. Song, H. R. Cheng, Y. H. Li, X. L. Yu, M. P. Zheng, M. K. Zhu, Y. D. Hou, *J. Eur. Ceram. Soc.* **2024**, 44, 1588.

[25] C. H. Zhao, S. Gao, T. N. Yang, M. Scherer, J. Schultheiss, D. Meier, X. L. Tan, H. J. Kleebe, L. Q. Chen, J. Koruza, J. Roedel, *Adv. Mater.* **2021**, 33, 2102421.

[26] X. Y. Dong, T. F. Hu, X. J. Wu, J. Yin, Z. Q. Fu, J. G. Wu, *SusMat.* **2023**, 4, 116.

[27] M. Acosta, L. A. Schmitt, L. Molina-Luna, M. C. Scherrer, M. Brilz, K. G. Webber, M. Deluca, H. J. Kleebe, J. Rödel, W. Donner, *J. Am. Ceram. Soc.* **2015**, 98, 3405.

[28] J. Zhang, Z. Pan, F. F. Guo, W. C. Liu, H. P. Ning, Y. B. Chen, M. H. Lu, B. Yang, J.

Chen, S. T. Zhang, X. R. Xing, J. Rödel, W. W. Cao, Y. F. Chen, *Nat. Commun.* **2015**, 6, 6615.

[29] T. Zheng, Y. G. Yu, H. B. Lei, F. Li, S. J. Zhang, J. G. Zhu, J. G. Wu, *Adv. Mater.* **2022**, 34, 2109175.

[30] J. H. Gao, Y. Wang, Z. X. He, Y. B. Liu, D. Wang, L. Jin, T. X. Zhao, L. S. Zhong, X. B. Ren, *Adv. Funct. Mater.* **2019**, 29, 1807162.

[31] C. Neusel, H. Jelitto, D. Schmidt, R. Janssen, F. Felten, G. A. Schneider, *J. Eur. Ceram. Soc.* **2015**, 35, 113.

[32] L. F. Zhu, S. Q. Deng, L. Zhao, G. Li, Q. Wang, L. H. Li, Y. K. Yan, H. Qi, B. P. Zhang, J. Chen, J. F. Li, *Nat. Commun.* **2023**, 14, 1166.

[33] Z. Q. Lv, T. Lu, Z. Liu, T. F. Hu, Z. C. Hong, S. B. Guo, Z. Q. Xu, Y. X. Song, Y. H. Chen, X. Y. Zhao, Z. S. Lin, D. H. Yu, Y. Liu, G. S. Wang, *Adv. Energy Mater.* **2024**, 14, 1304291.

[34] H. Simons, J. Daniels, W. Jo, R. Dittmer, A. Studer, M. Avdeev, J. Rödel, M. Hoffman, *Appl. Phys. Lett.* **2011**, 98, 3, 082901.

[35] M. Shen, L. W. Hu, L. Li, C. Zhang, W. R. Xiao, Y. J. Zhang, Q. F. Zhang, G. Z. Zhang, S. L. Jiang, Y. Chen, *J. Eur. Ceram. Soc.* **2021**, 41, 3379.

[36] Y. H. Shen, L. K. Wu, J. H. Zhao, J. J. Liu, L. M. Tang, X. Q. Chen, H. H. Li, Z. Su, Y. Zhang, J. W. Zhai, Z. B. Pan, *Chem. Eng. J.* **2022**, 439, 135762.

[37] F. Li, L. Jin, Z. Xu, S. J. Zhang, *Appl. Phys. Rev.* **2014**, 1, 011103.

We present a novel strategy to enhance the dielectric energy-storage performance by constructing a dual-phase structure through in-situ phase separation. By capitalizing on the synergistic effects of the dual perovskite structure configuration, we achieve a record-high energy density of 23.6 J cm^{-3} with an efficiency of 92% in a bulk ceramic capacitor.

Ultrahigh Energy-Storage in Dual-Phase Relaxor Ferroelectric Ceramics

Xin Xiong, Hui Liu, Ji Zhang, Lucas Lemos da Silva, Zhonghui Sheng, Yonghao Yao, Ge Wang, Manuel Hinterstein, Shujun Zhang, and Jun Chen**